

Single-bubble and multi-bubble cavitation in water triggered by Laser-driven focusing shock waves

D. Veysset,^{1,2} U. Gutiérrez-Hernández,³ L. Dresselhaus-Cooper,^{1,2} F. De Colle,³ S. Kooi,² K. A. Nelson,^{1,2} P. A. Quinto-Su,^{3,*} and T. Pezeril^{4,†}

¹*Department of Chemistry, Massachusetts Institute of Technology, Cambridge, MA 02139, USA*

²*Institute for Soldier Nanotechnologies, Massachusetts Institute of Technology, Cambridge, MA 02139, USA*

³*Instituto de Ciencias Nucleares, Universidad Nacional Autónoma de México,*

Apartado Postal 70-543, 04510 Cd. Mx., México

⁴*Institut Molécules et Matériaux du Mans, UMR CNRS 6283, Université du Maine, 72085 Le Mans, France*

In this study a single laser pulse spatially shaped into a ring is focused into a thin water layer, creating an annular cavitation bubble and cylindrical shock waves: an outer shock that diverges away from the excitation laser ring and an inner shock that focuses towards the center. A few nanoseconds after the converging shock reaches the focus and diverges away from the center, a single bubble nucleates at the center. The inner diverging shock then reaches the surface of the annular laser-induced bubble and reflects at the boundary, initiating nucleation of a tertiary bubble cloud. In the present experiments, we have performed time-resolved imaging of shock propagation and bubble wall motion. Our experimental observations of single-bubble cavitation and collapse and appearance of ring-shaped bubble clouds are consistent with our numerical simulations that solve a one dimensional Euler equation in cylindrical coordinates. The numerical results agree qualitatively with the experimental observations of the appearance and growth of dense ring-shaped bubble clouds at the smallest laser excitation rings. Our technique of shock-driven bubble cavitation opens novel perspectives for the investigation of shock-induced single-bubble or multi-bubble sonoluminescence phenomena in thin liquids.

I. INTRODUCTION

Liquids can withstand tensions due to intermolecular attractive potentials up to a tensile limit above which liquids rupture and bubbles nucleate. This limit varies depending on many factors, including the nature of the liquid, the purity of the liquid, as impurities drastically lower the limit through heterogeneous nucleation, the characteristics of the container [1], and the rate at which the tensile force is applied [2–4]. Water, in particular, has a wide range of measured tensile limits (from few to hundred negative MPa) that depend strongly on the rate at which the tensile force is applied [2–4]. Bubble generation, or cavitation, upon liquid rupture has implications in a variety of areas in technology and fundamental science. For instance, cavitation has been proposed as a damage mechanism for traumatic blast injury but the phenomenon is still poorly understood due to the difficulty for real-time observations [5]. In addition, the extreme conditions of pressure and temperature reached during bubble collapse are of great interest for chemists that investigate chemical reactions under the influence of sound [6]. There is therefore a clear need for reproducing the conditions for reliable bubble generation in the laboratory to allow systematic observations and studies of cavitation phenomena. Typically, cavitation bubbles are generated upon reflection of shock waves at a liquid-gas interface [4] or upon interaction of shock waves [7, 8]. In

this work we are interested in pursuing the shock-focusing configuration introduced by Pezeril et al. where a picosecond laser pulse shaped into a ring [9–12] is focused into a thin absorbing liquid sample to create high amplitude converging shock waves. This configuration enables the generation and the real-time observation of propagating shock waves as well as the dynamics of cavitation bubbles free of any interaction with the laser source, contrarily to laser cavitation experiments [13–15]. A few nanoseconds after the shock converges at the center of the ring, a bubble nucleates at the focus as the shock rebounds and diverges away from the center. The central bubble nucleation at the shock focus is a consequence of the Gouy phase shift, a well-known occurrence that has been observed through imaging of converging electromagnetic or acoustic waves [9]. In addition to the central bubble dynamics, we also observe the inner shock reflection at the annular laser-induced bubble and the subsequent nucleation of a tertiary bubble cloud.

In the present work, we expand the initial study on laser ring excitation [9–11] by exploring longer time delays in order to observe the dynamics of nucleated bubbles. We also model the shock wave propagation and focusing to quantify the effect of the laser ring radius on the negative pressure reached at the center.

The paper is organized in the following way. First, we describe the experimental setup and show the results of bubble nucleation from single-shot experiments. Second, we study the effects of varying the laser ring radius on bubble nucleation using stroboscopic imaging. Finally, we discuss our numerical simulations on the shock dynamics obtained from a one-dimensional axisymmetric Euler solver.

*Electronic address: pedro.quinto@nucleares.unam.mx

†Electronic address: thomas.pezeril@univ-lemans.fr

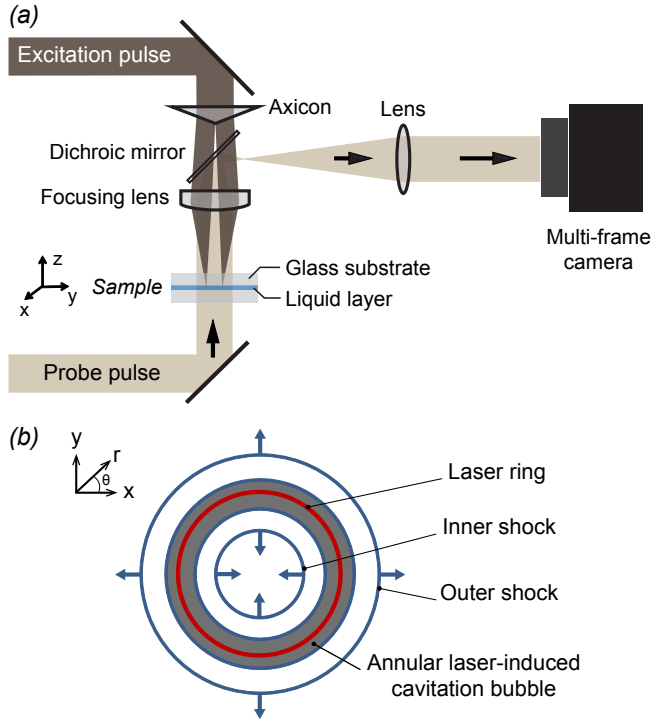


FIG. 1: (a) Experimental setup. An axicon combined with a lens is used to focus a laser excitation pulse as a ring at the sample location. The sample is illuminated by a probe pulse and imaged with high magnification on a multi-frame camera. (b) After laser absorption by the liquid sample, two in-plane counter-propagating shock waves are launched and remain mostly confined within the liquid layer. An expanding annular laser-induced cavitation bubble is nucleated upon laser irradiation.

II. SINGLE SHOT MULTI-FRAME IMAGING, EXPERIMENTAL SETUP AND RESULTS

The experimental setup is depicted in Fig. 1(a). A 150-ps duration, 800-nm wavelength, laser pulse delivered by an amplified Ti:sapphire system is focused into a 10 μm -thick liquid layer as described in [9–11]. The thin liquid layer consists of a suspension of carbon nanoparticles in water (India ink diluted to yield 2% weight carbon concentration). The layer is confined between two glass windows separated by a polymer spacer. The laser excitation pulse is shaped into a ring of 95 μm in radius in the plane of the liquid layer using a 0.5° axicon and a 3 cm focal length achromatic doublet as sketched in Fig. 1(a). After each shot of the laser excitation pulse, the sample is moved using a motorized stage to an undisturbed area in order to avoid remnant bubbles.

The time-resolved images are obtained through high-speed imaging. The high-frame-rate camera (SIMX 16, Specialized Imaging) that is used in the experiment can acquire 16 frames on a single shot, with tunable exposure time and tunable time interval between frames. As an

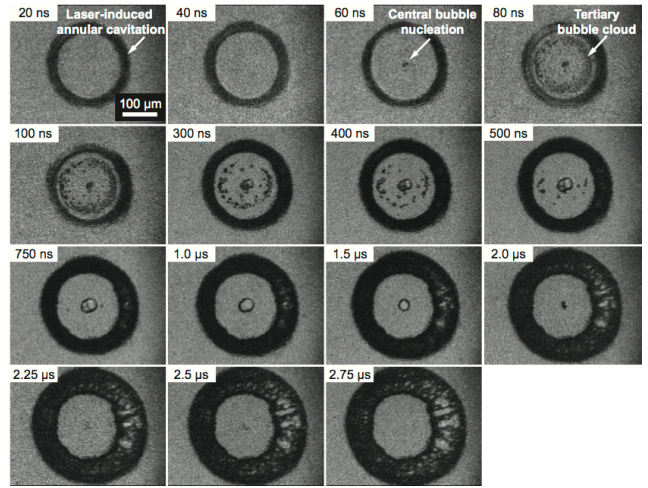


FIG. 2: Single-shot frames recorded for an excitation pulse of 0.5 mJ and a laser ring of 95 μm radius. The bubble formation at the vicinity of the annular bubble and the collapse dynamics of the central bubble are clearly apparent on this sequence of time resolved images.

illuminating probe, we use a 640 nm wavelength laser (Cavilux, Cavitair Ltd) of 30 μs pulse duration, which is longer than the total time required to acquire the 16 frames on the high-frame-rate camera.

Following laser absorption by the carbon nanoparticles in the liquid and subsequent vaporization, two counter-propagating shock waves are launched laterally within the liquid layer. The inner-propagating wave converges towards the center while the outer-propagating wave diverges, as sketched in Fig. 1(b). The converging shock accelerates upon convergence and increases in amplitude as it focuses towards the center of the ring. The diverging shock decreases in strength because of the combined effects of cylindrical divergence and attenuation. The rather efficient shock confinement within the liquid layer is ensured by the acoustic impedance mismatch between the liquid and the solid glass substrates [16].

Figure 2 shows a representative sequence of frames illustrating the bubble dynamics, recorded using a laser excitation energy of 0.5 mJ and a ring radius of 95 μm . The exposure time of each frame is set to 5 ns for frames 1 to 6 and 10 ns for the following frames. The shocks are not visible in these images, but based on previous work [9] on shock trajectories in this configuration, we expect the shock to reach the focus within 50 ns. At 60 ns, about 10 ns after shock focus, we observe the onset of bubble cavitation and growth at the center, while the rebounding inner diverging shock diverges toward the annular laser-induced bubble. The following five frames show the appearance and evolution of a nucleated tertiary bubble cloud due to the inner shock being reflected at the annular laser-induced bubble. Finally, the tertiary bubbles disappear within a few hundreds of nanoseconds whereas the central bubble collapses in a timescale of 1–2

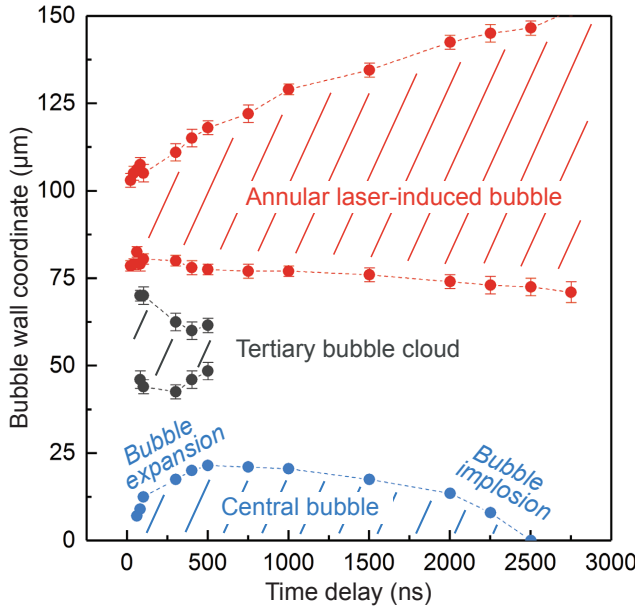


FIG. 3: Bubble walls trajectories extracted from the frames displayed in figure 2. The two stages of the central bubble wall trajectory (expansion and collapse) have analogies with the classical Rayleigh-Plesset bubble dynamics well-established in single bubble sonoluminescence [17].

microseconds.

To obtain the trajectories of the bubble walls, we extract the positions of the bubble boundaries from each of the frames presented in Fig. 2. The extracted trajectories are shown in Fig. 3. From the trajectories of the bubble walls, in particular the trajectory of the central bubble, we estimate the bubble wall average speed during the bubble expansion (first stage) and during the bubble collapse (second stage). The two stages of bubble motion have noticeable different average speeds, $v_{expansion} \sim 40 \mu\text{m}/\mu\text{s}$ and $v_{collapse} \sim 10 \mu\text{m}/\mu\text{s}$. The asymmetry in the bubble wall motion during each of the expansion and collapse stages calls for a comparison with the classical single bubble wall motion in a liquid driven by an external acoustic field. In the latter situation, the nonlinear 3D Rayleigh-Plesset equations models accurately the first stage of smooth expansion and the second stage of violent collapse of the single bubble motion, which leads to the observation of sonoluminescence [17]. As a comparison, the average bubble wall speed in sonoluminescence is in the range of $v_{expansion} = 3 \mu\text{m}/\mu\text{s}$ and $v_{collapse} = 10 - 20 \mu\text{m}/\mu\text{s}$. Our results suggest that in the present experimental situation the first stage of bubble expansion is more violent than the second stage of bubble collapse, which does not match the well-established Rayleigh-Plesset 3d model used in sonoluminescence but is consistent with the slower collapse of bubbles in thin liquids modeled with a 2D Rayleigh-Plesset equation [18]. Hence, these estimations indicate that the conditions for

the observation of the sonoluminescence phenomena are probably not fulfilled here. Even though our experimental attempts to observe sonoluminescence in our specific cylindrical configuration of bubble implosion were unsuccessful so far, these results of shock-driven bubble creation and implosion open novel perspectives related to the sonoluminescence phenomena.

III. SINGLE SHOT STROBOSCOPIC IMAGING, EXPERIMENTS VARYING THE LASER RING RADIUS

Experiments varying the laser excitation ring radius R are performed to observe the effect of radius on the tertiary bubble cloud for a constant laser excitation energy density - i.e. fluence. Such single-shot experiments were performed on a pump-probe stroboscopic manner from two distinct electronically time delayed laser systems. In these stroboscopic experiments, the dynamics are imaged with strobe photography by changing the time delay between the excitation pump pulse and the imaging probe pulse. The experimental setup for the stroboscopic measurements is described in [8] and it is similar to that shown in Fig. 1. For the excitation pulse, we used a Nd:YAG laser (New Wave, Solo PIV) with a duration of 6 ns and a wavelength of 532 nm. The pump excitation laser pulse is shaped with a computer-controlled spatial light modulator (SLM) to allow a straightforward modification of the laser ring radius at the focus of a $10 \times, 0.4 \text{ NA}$ microscope objective. A second frequency-doubled Nd:YAG laser (New Wave, Solo PIV) is used for probe illumination at a well defined time delay to capture

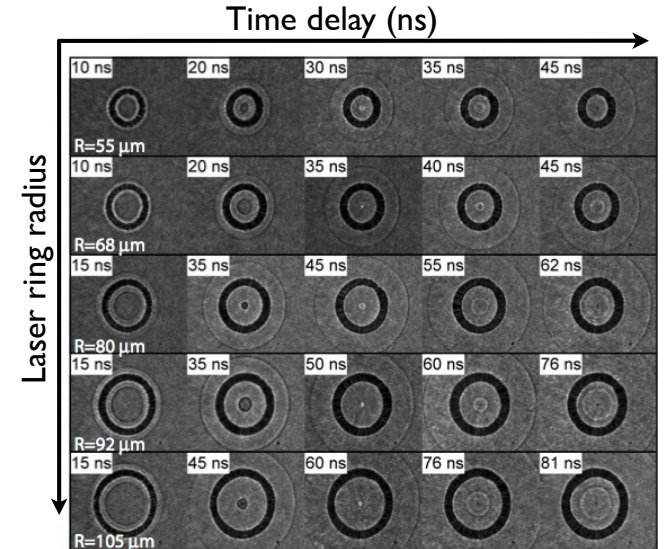


FIG. 4: Single-shot stroboscopic time-resolved images recorded for different laser ring radii $R = 55, 68, 80, 92, 105 \mu\text{m}$. Each individual frame has a width of $410 \mu\text{m}$. The central column shows the instant of inner shock focus.

the dynamics of the events. The beam is focused into a dye cell (Exciton Rhodamine 698 diluted in methanol) to excite emission centered at 698 nm. The emitted 698 nm probe pulses are coupled to an optical fiber that directs the light into the condenser of the microscope to illuminate the sample. The single-shot events are imaged with an ICCD camera (Andor, IStar). The studied liquid is undiluted ink (T6643 Epson, magenta, $< 80\%$ water by weight, 1.08 relative density) of 19 μm thickness confined in between two glass substrates. The studied laser ring radii R are 55, 68, 80, 92, and 105 μm . The energy per excitation pulse is adjusted to maintain a constant fluence for each laser ring radius. The diffracted energy at the largest radius is 222 μJ . The energy for the other radii are adapted to maintain a constant laser fluence, assuming a laser ring width of the diffraction-limited spot size.

Figure 4 shows the dynamics of the annular laser-induced bubbles and the shock-induced central bubbles as a function of laser radius. Each row shows a different value for the laser ring radius R (55, 68, 80, 92, and 105 μm), with the smallest being at the top row, while the columns corresponds to different time delays. The central column in Fig. 4 shows images of the inner shock that focuses at the center of the laser ring. As expected, the time for shock focusing increases when the laser ring radius R increases. At longer time delays, the diverging inner shock and a cavitation bubble growing at the center can be seen on the right column of images displayed in Fig. 4. Once the inner diverging shock reaches the wall of the annular laser-induced bubble, it is reflected as a tensile shock wave and travels back toward the center of the ring (not shown here).

As evidenced in Fig. 5, a tertiary bubble cloud such as the one observed earlier in Fig. 2, appears on a time scale following the reflection of the diverging inner shock at the annular laser-induced bubble wall. These observations suggest that the rebounding shock wave becomes negative upon reflection at the annular laser-induced bubble wall due to the acoustic impedance mismatch between the liquid and the bubble, which leads to the nucleation of a tertiary bubble cloud. We also observe that the nucleated bubble clouds are denser for smaller laser excitation rings, see the frames bounded by dashed lines in Fig. 5. For instance, for the laser ring radius R of 55 μm and 68 μm , the bubble clouds fully fill the space enclosed by the annular laser-induced bubble, see at 132 ns time delay in Fig. 5. We also speculate that the annular laser-induced bubble increases the lifetime of the nucleated bubble clouds [19] by shielding the microbubbles from the liquid static pressure. It seems as well that multiple bubble clouds are nucleated as the reflected inner tensile shock focuses towards the center. Most probably, the bubble clouds in Fig. 5 have a sufficiently long lifetime for several bubble clouds to appear simultaneously while the shock bounces back and forth inside the annular laser-induced bubble.

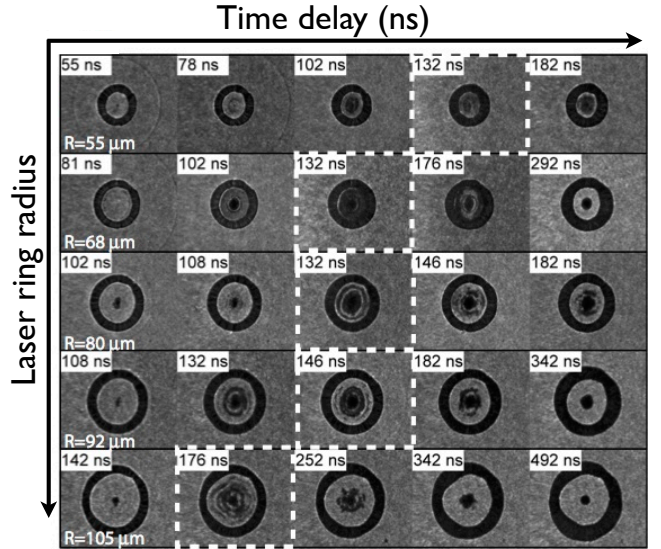


FIG. 5: Stroboscopic time-resolved images recorded such as in Fig. 4, at longer timescales. A bubble cloud appear after reflection of the inner shock at the annular laser-induced bubble. The dashed frames highlight the instant when the bubble density appears to be maximum. Each individual frame has a width of 410 μm .

IV. NUMERICAL SIMULATIONS

Our numerical simulations intend to describe the inner shock wave propagation and focusing within the laser-induced bubble ring to model the conditions of the appearance of single-bubble and bubble clouds arising from the tensile component of the inner shock wave. Additional effects are not considered in our simulations, including shielding by the annular laser-induced bubble [19] and possible shear-induced nucleation due to the interaction between the shock and the glass surface of the substrate holding the liquid film [16, 20]. In the experiments, differences between liquid compositions and layer thicknesses should result in different pressure thresholds for bubble nucleation through heterogeneous nucleation.

We simulate the shock wave evolution by solving a single component Euler equation with the stiffened equation of state for water [21], assuming for simplicity infinite acoustic impedance mismatch between water and the glass substrate. We run a series of numerical simulations by using the *Mezcal* code, an Eulerian code which integrates the hydrodynamics equations by a second order, in space and time, Godunov method [22, 23]. The code has been extensively used to study fluid dynamics problems. The hydrodynamics equations are integrated in conservative form by solving equations regulating the evolution of mass, momentum, and total energy, with the total energy defined as the sum of thermal and kinetic energy, i.e. $e = e_k + e_{\text{th}}$, and the thermal energy related to

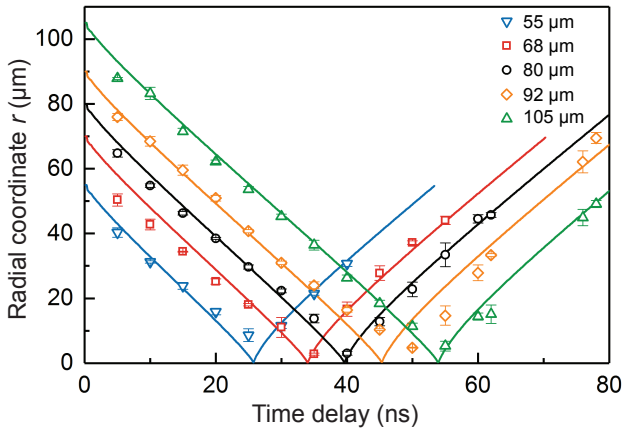


FIG. 6: Numerical simulations of the inner shock trajectories for several laser ring radius of $R_{sim} = 55, 70, 80, 90, 105 \mu\text{m}$ and an initial pressure of 2 GPa. The symbols correspond to the inner shock trajectories extracted from Fig. 4 for different laser ring radius.

the fluid pressure by the following equation of state,

$$e_{th} = \frac{p}{\Gamma - 1} + \Gamma p_{\infty}, \quad (1)$$

being $p_{\infty} = 3.07 \times 10^8 \text{ Pa}$, and the adiabatic index $\Gamma = 7.15$ [8, 24]. The speed of sound is then defined in the code by $c_s = \sqrt{\Gamma(p + p_{\infty})/\rho}$.

The simulations include a one-dimensional, cylindrically-symmetric uniform grid with radial coordinate r in the range of 0-150 μm with steps of 5 μm resolved by 6000 cells, corresponding to a spatial resolution of $2.5 \times 10^{-2} \mu\text{m}$ per cell. The computational region is initialized by setting an uniform density of 1000 kg/m^3 and a pressure of 10^5 Pa . We assume that the energy of the laser beam is homogeneously deposited on a ring of radius R and width $\Delta R = 1.6 \mu\text{m}$, similar to the diffraction limited spots of the microscope objectives used in this study. We initialize the impulse pressure to a value $P = 2 \text{ GPa}$ to interpret our experimental observations in Fig. 5. We run several models with R varying from 15 to 110 μm . The evolution of the shock is followed during 1400 ns.

The simulations of the trajectories of the inner shock waves for different laser ring radii are plotted in Fig. 6. The continuous lines represent the results of simulations for several laser excitation radii R_{sim} of 55, 70, 80, 90, and 105 μm and an initial pressure of 2 GPa while the symbols corresponds to the radial position r of the inner shock waves as they propagate toward and later away from the center ($r = 0 \mu\text{m}$) extracted from the images displayed in Fig. 4. There is an excellent agreement between the numerical simulations and the experimental results which confirms the accuracy of the modeling.

The simulations of the time evolution of the spatial pressure profiles for a laser ring radius R of 50 μm , from

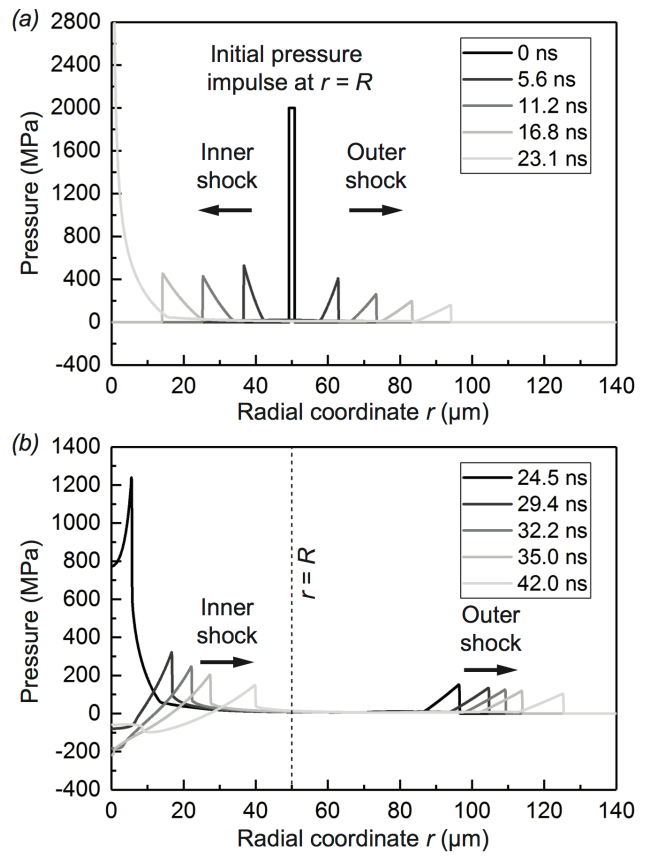


FIG. 7: Numerical simulations of the spatial pressure profiles at different times during shock propagation of both, inner and outer shock waves, departing from the laser ring coordinate $r = R = 50 \mu\text{m}$. (a) The top figure shows both spatiotemporal pressure profiles until the time of shock focusing. (b) The bottom figure shows the spatiotemporal pressure profiles of both inner and outer shock waves at later times after shock focusing. The appearance of a tensile tail on the inner shock spatial profile, right after shock focusing, arise from the acoustic discontinuity at the center.

$t = 0 \text{ ns}$, corresponding to the initial pressure impulse of 2 GPa driven by the laser to the instant at which the inner shock focuses at the center are shown in Fig. 7(a). The joint effects of the spatial overlap of the inner shock wave at the center of the ring and the geometrical in-plane confinement of the cylindrical shock wave while approaching the center, entail a sudden and giant increase of the shock pressure right at the shock focus at $r = 0 \mu\text{m}$ to 40 GPa (the vertical range is limited to 2 GPa in Fig. 7(a)). On the other hand, the geometrical divergence of the outer shock wave induces a gradual decrease in amplitude. Figure 7(b) shows the simulated shock pressure profiles at longer times after the inner shock has focused and diverged away from the center. The acoustic discontinuity at the shock focus, an occurrence of the Gouy phase shift [9], is responsible for the transformation of the unipolar shape of the incoming spatial shock profile

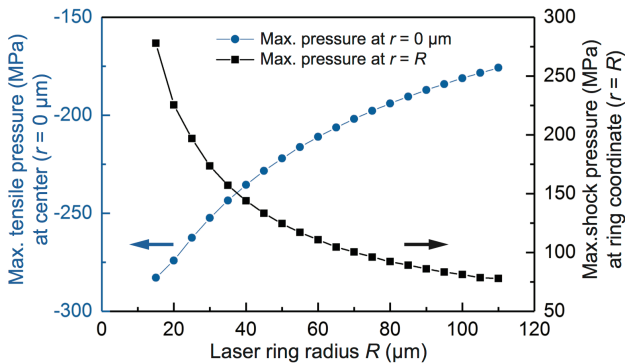


FIG. 8: (left axis) Maximum tension pressure as a function of the laser ring radius R , these are reached at the center ($r = 0 \mu\text{m}$) shortly after the inner shock focuses. (right axis) Maximum positive pressure as the inner shock rebounds and reaches original position $r = R$.

into a bipolar spatial shock profile with a tensile pressure tail. The simulations in Fig. 7(b) confirm that upon crossing the shock focus, the inner shock profile becomes bipolar with a characteristic positive pressure front and a tensile pressure tail. The tensile pressure tail, which in the equation of state corresponds to a negative pressure, can stretch the liquid below vaporization resulting in bubble cavitation right at the shock focus where the tensile pressure is maximum, as evidenced in our experimental observations of the appearance of a central bubble at the shock focus. In the simulations displayed in Fig. 7(b), we also notice that after reaching a maximum tensile value at the center at $r = 0 \mu\text{m}$, the tension at the center decreases as the shock wave propagates away, and the minimum value of the pressure shifts and extends to larger values of r , see Fig. 7(b) at 42 ns, which indicates that the bubble cavitation effect at the center can probably spread at long distances to the focus.

In order to interpret the behavior of the appearance of the central bubble, we have performed numerical simulations of the tensile pressure at the center for different values of the laser excitation radius R . The plot of the largest tensile pressures reached at the center at $r = 0 \mu\text{m}$ as a function of the laser excitation radius R is shown in Fig. 8(left axis). The maximum tensile pressure is reached for the smallest R and decreases monotonically for larger values of R . In the experiment, the liquid is expected to break at moderate negative pressures due to heterogeneous nucleation. Therefore, the central cavitation bubble should appear as soon as the value of the pressure drops below the vapor pressure, which occurs a few nanoseconds after shock focusing. As seen in the simulations of Fig. 8(left axis), the tensile pressure tail of the focusing shock wave is well below the vapor pressure and should induce bubble cavitation at the center for any given R , however, the tensile pressure being higher for small R , the bubble cavitation effect at the center is

expected to be more efficient for small R .

Similarly, in order to model the conditions of the appearance of the bubble cloud, we have performed numerical simulations of the inner shock wave propagation away from the shock focus, until it reaches the annular laser-induced bubble wall where it gets converted into a tensile wave. Figure 8(right axis) shows the maximum value of the pressure of the inner shock front right at the laser ring coordinate $r = R$, where it gets reflected by the laser-induced annular bubble and converted into a tensile wave, for different values of the laser excitation radius R . For simplicity, we assume that the laser-induced annular bubble does not expand. From the simulations displayed in Fig. 8(right axis), it appears that smaller radius R lead to higher shock pressures at the ring coordinate. Hence, we expect stronger reflected tensile shock waves for smaller laser radii which should most likely give rise to denser bubble clouds. This is qualitatively confirmed by our experimental observations of bubble clouds for different radius R in Fig. 5, where denser tertiary bubble clouds are observed for smaller laser excitation rings.

V. CONCLUSION

We have experimentally observed several transient phenomena such as single-bubble cavitation as well as bubble cloud nucleation as a result of the propagation and focusing of a cylindrical shock wave.

Our experimental results are supported by numerical modeling, which have shown that, as expected, the rebounding inner shock stretches the liquid at the center of the ring. This results in the appearance of a single cavitation bubble at the center which expands and collapses in a few microseconds. The nucleation of a tertiary bubble cloud, resulting from the reflection of the inner diverging shock at the annular laser-induced bubble, is experimentally observed and is supported by our numerical modeling as well. The experimental observations of denser bubble clouds for smaller laser ring radii agree qualitatively with our simulations. Our findings shed light on shock-induced cavitation and bubble nucleation.

Ultrasound-driven sonoluminescence in confined liquid geometries like microfluidic channels has been observed in [25]. So far our experimental attempts for the observation of sonoluminescence in our specific cylindrical configuration and liquid confinement of bubble implosion has been unsuccessful. At the moment, the present work of converging shock-driven bubble creation and implosion opens novel perspectives and challenges in the frame of high amplitude shock waves in liquids and energetic cavitation [14, 15, 28–30].

Acknowledgments

Work partially supported by the following grants: U.S. Army Research Office through the Institute for Soldier Nanotechnologies, contract number W911NF-13-D-0001, Office of Naval Research DURIP grant number N00014-

13-1-0676, CONACYT contract number 253706, 253366, 269314, DGAPA-UNAM, (PAPIIT) contract number IN104415, IN117917, IA103315, and CNRS (Centre National de la Recherche Scientifique) under PICS contract (Projet International de Coopération Scientifique).

[1] E. Herbert, S. Balibar, F. Caupin, *Phys. Rev. E* **74**, 041603 (2006).

[2] A. Maxwell, C. Cain, T. Hall, J. Brian Fowlkes, Z. Xu, *Ultrasound Med. Biol.* **39**, 449 (2013).

[3] A. Arvengas, K. Davitt, F. Caupin, *Rev. Sci. Instrum.* **82**, 034904 (2011).

[4] K. Ando, A.-Q. Liu, C.-D. Ohl, *Phys. Rev. Lett.* **109**, 044501 (2012).

[5] J. Goeller, A. Wardlaw, D. Treichler, J. O'Bruba, G. Weiss, *J. Neurotrauma*, **29**, 1970 (2012).

[6] K. S. Suslick, *Science* **247**, 1439 (1990).

[7] C. D. Ohl, S. W. Ohl, *Bubble Dynamics and Shock Waves*, Bubble Dynamics and Shock Waves, Springer Berlin Heidelberg, Can F. Delale (Ed.), pp. 331 (2013).

[8] P. A. Quinto-Su, K. Ando, *J. Fluid Mech.* **733**, R3 (2013).

[9] T. Pezeril, G. Saini, D. Veysset, S. Kooi, P. Fidkowski, R. Radovitzky, K. A. Nelson, *Phys. Rev. Lett.* **106**, 214503 (2011).

[10] D. Veysset, T. Pezeril, S. Kooi, A. Bulou, K. A. Nelson, *Appl. Phys. Lett.* **106**, 161902 (2015).

[11] D. Veysset, A. Maznev, T. Pezeril, S. Kooi, K. A. Nelson, *Sci. Rep.* **6**, 24 (2016).

[12] D. Veysset, A. Maznev, I. Veres, T. Pezeril, S. Kooi, A. Lomonosov, K. A. Nelson, *Appl. Phys. Lett.* **111**, 031901 (2017).

[13] C. D. Ohl, T. Kurz, R. Geisler, O. Lindau, W. Lauterborn, *Phil. Trans. R. Soc. Lond. A* **357**, 269 (1999).

[14] C. Bell, J. Landt, *Appl. Phys. Lett.* **10**, 46 (1967).

[15] A. Vogel, S. Busch, U. Parlitz, *J. Acoust. Soc. Am.* **100**, 148 (1996).

[16] L. Dresselhaus-Cooper, J. E. Gorfain, C. T. Key, B. K. Ofori-Okai, S. J. Ali, D. J. Martynowich, A. Gleason, S. Kooi, K. A. Nelson, [arXiv:1707.08940](https://arxiv.org/abs/1707.08940).

[17] M. P. Brenner, S. Hilgenfeldt, D. Lohse, *Rev. Mod. Phys.* **74**, 425 (2002).

[18] P.A. Quinto-Su, K.Y. Lim, and C.D. Ohl, *Phys. Rev. E* **80**, 047301 (2009).

[19] N. Bremond, M. Arora, C.D. Ohl, and D. Lohse, *Phys. Rev. Lett.* **96**, 224501 (2006).

[20] K. Ando, A.-Q. Liu, and C.D. Ohl, *Proceedings of the 8th International Symposium on Cavitation CAV 2012*, paper 181 (2012).

[21] J.P. Cocchi, R. Saurel, and J.C. Loraud, *Shock Waves*, **5**, 347-357 (1996).

[22] F. De Colle, A. C. Raga, *Astron. Astrophys.* **449**, 1061 (2006).

[23] F. De Colle, A.C. Raga, A. Esquivel, *Astrophys. J.* **689**, 302 (2008).

[24] K.M. Shyue, *J. Comp. Phys.* **142**, 208 (1998).

[25] Tandiono, S.-W. Ohl, D. S. W. Ow, E. Klaseboer, V. V. Wong, R. Dumke, C.-D. Ohl, *PNAS* **108**, 5996 (2011).

[26] O. Antonov, L. Gilburd, S. Efimov, G. Bazalitski, V. Tz. Gurovich, Ya. E. Krasik, *Phys. Plasmas* **19**, 102702 (2012).

[27] M. Nitishinskiy, S. Efimov, D. Yanuka, V. Tz. Gurovich, and Ya. E. Krasik, *Phys. Plasmas* **23**, 103507 (2016).

[28] G. Sankin, W. Simmons, S. Zhu, P. Zhong, *Phys. Rev. Lett.* **95**, 034501 (2005).

[29] O. Antonov, L. Gilburd, S. Efimov, G. Bazalitski, V. Tz. Gurovich, Ya. E. Krasik, *Phys. Plasmas* **19**, 102702 (2012).

[30] M. Ramsey, R. Pitz, *Phys. Rev. Lett.* **110**, 154301 (2013).